Nanoscale

Accepted Manuscript

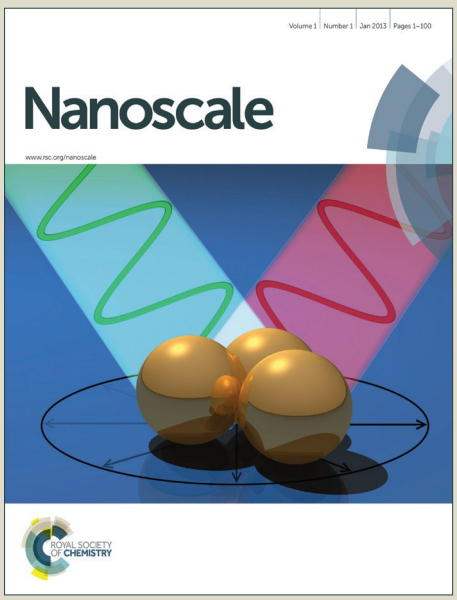

ROYAL SOCIETY OF CHEMISTRY

www.rsc.org/nanoscale

Journal Name

ARTICLE

Au_{25} clusters functionalized metal-organic nanostructures for magnet targeted photodynamic/photothermal therapy triggered by a single 808 nm near-infrared light

Received 00th January 20xx,
Accepted 00th January 20xx

DOI: 10.1039/x0xx00000x

www.rsc.org/

Dan Yang, Guixin Yang, Shili Gai,* Fei He, Guanghui An, Yunlu Dai, Ruichan Lv, and Piaoping Yang*

The near infrared (NIR) light-induced cancer therapy has gained considerable interest and pure inorganic anti-cancer platform usually suffers from the degradation issue. Here, we designed metal-organic frameworks (MOFs) of Fe_3O_4/ZIF-8-Au_{25} (IZA) nanospheres through a green and economic procedure. The encapsulated Fe_3O_4 nanocrystals not only produce hyperthemia upon NIR light irradiation to effectively kill tumor cells, but present targeting and MRI imaging functions. More importantly, the attached ultrasmall $Au_{25}(SR)_{18}^-$ clusters (about 2.5 nm) produce highly reactive singlet oxygen ($^1O_2$) to cause photodynamic effect through direct sensitization under NIR light irradiation. Meanwhile, the $Au_{25}(SR)_{18}^-$ clusters also give a hand to hyperthemia effect as a photothermal fortifier. This nanoplatform exhibits high biocompatibility and enhanced synergistic thepeutic effect superior to any single therapy, verified evidently by *in vitro* and *in vivo* assay. This imaging-guided therapy based on a metal-organic framework may stimulate interest in developing other kinds of meatal-ortanic materials with multifunctions for tumor diagnosis and therapy.

Introduction

As a vibrantly class of crystalline materials, metal-organic frameworks (MOFs) are constructed by metal ion/ion clusters and organic bridging ligands.[1] up to now, this kind of material unquestionably has an enormous potential in many practical fields, such as selective gas adsorption and separation,[2,3] optical devices,[4–6] sensors,[7,8] drug delivery,[9–12] and catalysis,[13,14] owing to their uniform but adjustable cavities and tailorable chemistry.[15,16] Among all the MOFs materials, nanoscale metal-organic frameworks (NMOFs) have recently emerged as a promising diagnostic agent and carrier nanoplatform for disease therapy.[17–19] For instance, zeolite imidazolate frameworks (ZIFs), which have the merits of drug carrier and conventional MOFs, can be really applied as a potential drug delivery carrier for therapy and diagnosis.[20–22] Similar to the already existing carrier for cancer therapy and imaging, the nanocomposite is usually well dispersed in the aqueous solution, having large specific surface area for loading drug molecules and adhered to functional molecules, so that it shows high reactivity in the synthetic modifications for future biomedical applications. ZIFs also take advantage of its crystalline and porous structure to provide a pathway for facile diffusion of substance (such as $^1O_2$, drug molecules) out of the ZIF interior to exert their cytotoxic effects on cancer cells, admirable hydrophilia and intersecting three-dimensional structure of the aluminosilicate zeolite like the conventional MOFs.

To achieve special function like magnetic property, the coating of the magnetic materials such as Fe_3O_4 on the surface of preformed ZIFs is a preferred strategy. Importantly, the introduction of magnetic materials can not only strongly respond to the external field to provide magnetic targeting, but also favorably apply to magnetic resonance imaging (MRI) act as a T_2 contrast agent in the clinic application of cancer therapies. Notably, superior to molecular targeting, magnetic targeting based on physical interaction is not greatly limited by the specific receptor expression such as the patient-to-patient variation, or the non-specific expression of receptors in normal tissues.[23,24] Besides, the most interesting point is that iron oxide nanoparticles (IONPs) have been approved for clinic application by Food and Drug Administration (FDA) because the excess irons can be stored and processed by human body. After internalization by cells, IONPs stayed in endosomes and lysosomes are metabolized into elemental iron and oxygen by hydrolytic enzymes, where iron joins normal body stores. To date, most drug carrier system containing IONPs have been extensively studied due to not only some intrinsic merits including high biocompatibility, biodegradability, magnetic property and high chemical stability, but the capability to be used as NIR photoabsorbers and magnetic contrast agent, giving rise to NIR photothermal therapy and MR imaging for efficient tumor ablation and diagnostics.[25–27] Chu and co-

Key Laboratory of Superlight Materials and Surface Technology, Ministry of Education, College of Material Science and Chemical Engineering, Harbin Engineering University, Harbin, 150001, P. R. China. E-mail: yangpiaoping@hrbeu.edu.cn; gaishili@hrbeu.edu.cn

Electronic Supplementary Information (ESI) available: XRD patterns of the samples, FT-IR spectra of the samples, N_2 adsorption/desorption isotherm and pore size distribution, CLSM images of the HeLa cells incubated with culture and the sample under NIR irradiation, blood biochemistry and hematology data. See DOI: 10.1039/x0xx00000x

authors reported IONPs with various shapes can exhibit strong photothermal effect during red and NIR laser irradiation. Therefore, the strategy based on the magnetic targeting and hyperthermia treatment using IONPs is a promising cancer therapy route by applying an external magnetic field and remote controlled mode.[28]

We all know the importance of synthetic modifications to the surfaces of drug delivery carriers (DDCs) for the application in biomedicine field.[29] In recent years, to further enhance the therapeutic efficiency to cancer, numerous groups have reported diverse composites for drug release, photothermal therapy (PTT), radiation therapy, and photodynamic therapy (PDT).[30–34] Initially, small-molecule drugs (such as doxorubicin, Pt.), which arrive the diseased region through encapsulated or conjugated to internal domains of the carrier, are the mainstay in the cancer therapy.[35–38] But, this route can't perfectly achieve expected effect due to premature release of drug or cause harm to healthy cells in the cellular pathways. Thus, innovative studies in multimode therapy are stimulated in the clinic treatments. Following the deepening of research, the emergence of PTT, PDT, and combination with aforementioned drug treatment provide a new strategy for disease therapy. PTT and PDT are different forms of phototherapy. In PTT process, the PTT agent absorbs energy from photon and dissipates the absorbed energy by non-radiative decay like heating, which can cause the irreversible cell damage and subsequent tumor regression by increasing the temperature sufficiently in the tumor sites. At present, researchers have explored many light-absorbing species for PTT. Most of them base on inorganic nanomaterials including gold nanomaterials (Au nanoshells,[39,40] nanorods,[41] and nanocages[42,43]), carbon nanomaterials (carbon nanotube[44] and graphene[45]), palladium nanosheets,[46] iron oxide nanoparticles,[47–49] copper sulfide nanoparticles,[50,51] and others relied on organic polymeric nanoparticles covering polypyrrole (PPy)[52,53] and polyaniline.[54] However, the pure inorganic anti-cancer platform inevitably faces with some problems such as the degradation issue. Thus, developing other kinds of materials to overcome these drawbacks is highly desirable. As candidates, Inorganic-organic hybrid materials gain much attention as diagnostic agent and carrier platform due to their unique features. Furthermore, compared with individual mode, combined therapies of noninvasive PTT and PDT into a single system for cancer treatment acquire more and more attention owing to their enhanced therapeutic efficiency and reduced side effects.[55–59] The process of PDT also can result in the death of cancer cells using photosensitizer (PS) that selectively absorbs a particular wavelength of light to produce highly reactive oxygen species (ROS) such as free radicals or singlet oxygen ($^1O_2$), leading to toxicity to targeted cells.[60–63] So far, the PS for response to PDT have been widely reported including zinc phthalocyanine (ZnPc),[64,65] and the chlorine6 (Ce6).[46,66,67] Recently, a new PDT agent- $Au_{25}(SR)_{18}^-$ clusters (H-SR = phenylethanethiol or captopril) which can produce highly reactive singlet oxygen efficiently through direct sensitization under *vis*-NIR (532, 650, and 808 nm) irradiation has been reported.[68] Compared to conventional PS, $Au_{25}(SR)_{18}^-$ clusters exhibit as an ideal candidate as an efficient PS owing to its high stability, excellent water solubility, the presence of triplet excited states, and the long lifetime of the electronic excited states (on the order of a microsecond).[69,70]

In this paper, we fabricated a novel synergistic therapeutic system based on metal-organic frameworks (MOFs) of Fe_3O_4/ZIF-8-Au_{25} (IZA) nanospheres through a green and economic strategy of aqueous reaction between MeIM and zinc nitrate in the presence of premade negatively charged Fe_3O_4 nanocrystals at room temperature, which show remarkable anti-cancer therapeutic efficacy derived from the combined noninvasive PTT and PDT. It should be mentioned that we proposed a new idea for constructing multifunctional NMOFs structure by attaching novel PS agent as $Au_{25}(Capt)_{18}^-$ for biomedical application. On one hand, the $Au_{25}(Capt)_{18}^-$ clusters can be directly sensitized under 808 nm NIR irradiation to produce efficient ROS. On the other hand, the NMOFs material is a potential candidate for clinic application due to the large specific surface area which is advantageous to the functional modification. In addition, the magnetic property not only vertically give a hand for PTT effect through targeting remote control, but the magnet itself serve as a MR imaging agent to simultaneously achieve the aim of diagnosis and treatment. Our study highlights the effect of $Au_{25}(SR)_{18}^-$ clusters enhancement hyperthemia effect as a photothermal fortifier in PTT and demonstrates the importance of systematic design of nanoplatform to greatly enhance the antitumor efficacy. *In vitro* and *in vivo* assay has been employed to verify the imaging and anti-cancer efficacy.

Results and discussion

Phase, structure, and morphology. Fig. S1A gives the respective XRD pattern of ZIF-8, Fe_3O_4/ZIF-8, Fe_3O_4/ZIF-8-Au_{25} and Fe_3O_4. As shown, the XRD patterns of Fe_3O_4/ZIF-8 and Fe_3O_4/ZIF-8-Au_{25} are similar to that of pure ZIF-8, except for an obvious diffraction peak assigned to Fe_3O_4 (JCPDS No. 19-0629) at about 36°, indicating the successful introduction of Fe_3O_4 nanocrystals in the hetero-nanostructure. When $Au_{25}(Capt)_{18}^-$ clusters were attached onto the surface, the XRD pattern of as-obtained Fe_3O_4/ZIF-8-Au_{25} has almost not changed (Fig. S2Aa-c) compared to that of Fe_3O_4/ZIF-8 because the peak intensity of Fe_3O_4/ZIF-8-Au_{25} is relatively weaken to that of pure MOF material by several orders of magnitude (Fig. S1Ba-c). Thus, the diffraction peaks of hetero-nanostructures attributed to inorganic nanocrystals can hardly be observed, which is consistent with the FT-IR result (Fig. S2).

The mesostructured inorganic-organic Fe_3O_4/ZIF-8-Au_{25} nanocomposite was prepared *via* an aqueous reaction between MeIM and zinc nitrate in the presence of premade negatively charged Fe_3O_4 nanocrystals, and following electrostatic adsorption between ZIF-8 and $Au_{25}(Capt)_{18}^-$ clusters at room temperature. To achieve PDT, $Au_{25}(Capt)_{18}^-$ clusters with an average diameter of 2.5 nm (Fig. 1A, B) were introduced into the MOFs structures. As shown in Fig. 1C and D, Fe_3O_4 nanocrystals with a mean diameter of 10 nm were fabricated by a high temperature polyol reaction using PAA as

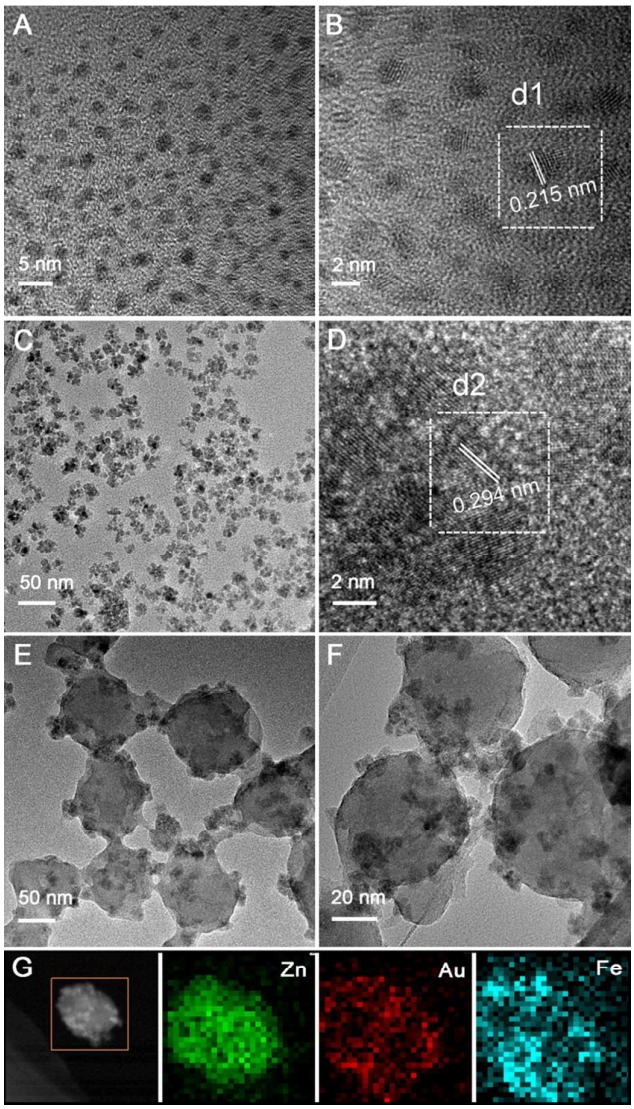

Fig. 1 TEM and HRTEM images of (A, B) $Au_{25}(Capt)_{18}^-$ clusters, (C, D) PAA-grafted Fe_3O_4 nanoparticles, (E, F) Fe_3O_4/ZIF-8-Au_{25} composite and (G) the elemental mapping images of Fe_3O_4/ZIF-8-Au_{25} (IZA).

a surfactant. The HRTEM images with two rectangle zones are given in Fig. 1B and Fig. 1D, respectively. As shown, the two typical lattice distances of 0.22 nm and 0.29 nm correspond to the (220) and (111) planes of $Au_{25}(Capt)_{18}^-$ clusters (JCPDS No. 65-8601) and Fe_3O_4 (JCPDS No. 19-0629), respectively. For the final product (Fig. 1E and 1F), the sample consists of well-dispersed nanoparticles with the mean size of 100 nm, and the attached nanoparticles can easily be found. The elemental mapping images (Fig. 1G) show the good distribution of the elements and the successful introduction of Au and Fe ions simultaneously.

Fe_3O_4/ZIF-8-Au_{25} composite has ordered porous structure and large specific surface area, which are proved by nitrogen adsorption–desorption isotherm (Fig. S3A). The curve exhibits type-IV hysteresis with a platform and a sharp increase in nitrogen uptake at high relative pressure P/P_0 of 0.9 and a hysteresis loop appearing at $P/P_0 > 0.3$ according to the IUPAC

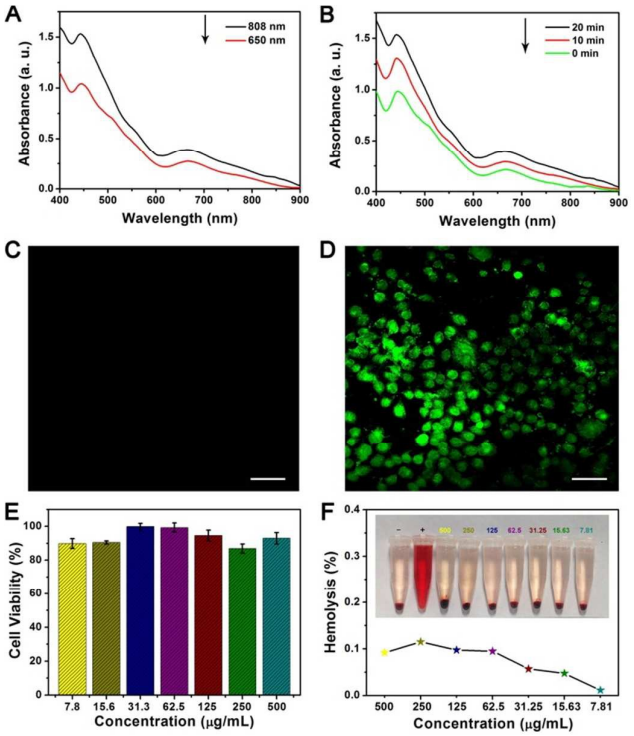

Fig. 2 (A) Absorption spectra of a DAB-containing solution of Fe_3O_4/ZIF-8-Au_{25} under 650 nm laser (0.5 W/cm^2) and 808 nm laser (0.5 W/cm^2); (B) Absorption spectra of Fe_3O_4/ZIF-8-Au_{25} in a DAB-containing solution at different irradiation time under 808 nm laser (0.5 W/cm^2); CLSM image of HeLa cells incubated (C) with Fe_3O_4/ZIF-8, (D) with Fe_3O_4/ZIF-8-Au_{25} under NIR irradiation. All the cells were marked with DCFH-DA. Scale bars for all images are 75 μm. (E) Cell viability for L929 cells incubated with Fe_3O_4/ZIF-8-Au_{25} with different concentrations for 24 h; (F) Hemolytic assay of Fe_3O_4/ZIF-8-Au_{25} to human red blood cells.

(International Union of Pure and Applied Chemistry), which are characteristics of typical mesoporous structure. The mesopore size distribution curve is given in Fig. S3B. The size distribution exhibits a sharp peak centered at around 3.7 nm, implying a uniform pore size. The respective BET surface area and total pore volume is calculated to be 1106 m^2/g and 7.9 cm^3/g.

ROS detection, biocompatibility and MR imaging. 3,3-diaminobenzidine (DAB) was used as a chemical probe to determine the generated $^1O_2$ of IZA (100 μg/mL Au) in aqueous media. Our group have reported that DAB has high selectivity to $^1O_2$ and reacts irreversibly with $^1O_2$ to lead to an increase in the DAB absorption at about 440 nm.[67] The singlet oxygen ($^1O_2$) generation capability of IZA was assessed by monitoring the time-dependent photo degradation of DAB upon 808 nm laser irradiation and examining the DAB absorption at 440 nm when exposed to the 650 nm laser or 808 nm at a power density of 0.5 W/cm^2 (Fig. 2A, B). The UV-*vis* absorbance intensity of IZA decreases obviously with the irradiation time due to the photo degradation of DAB. The result suggests the efficient generation of $^1O_2$ by IZA, and the $^1O_2$ production ability by IZA irradiated upon 650 nm laser light is weaker than that exposed to the 808 nm laser light, which is consistent with the result of strong absorption in the NIR region between 700 and 900 nm.

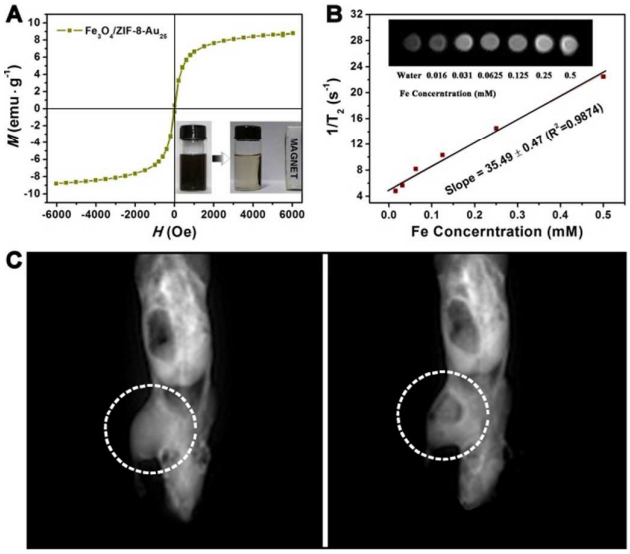

Fig. 3 (A) Field-dependent magnetization loop of the Fe_3O_4/ZIF-8-Au_{25} sample; (B) T_2-weighted MR images of Fe_3O_4/ZIF-8-Au_{25} nanocomposite recorded using a 3 T MR scanner; (C) MR imaging for *in vivo* mapping using Fe_3O_4/ZIF-8-Au_{25} sample. MR images were taken before (left) and after (right) injection of IZA.

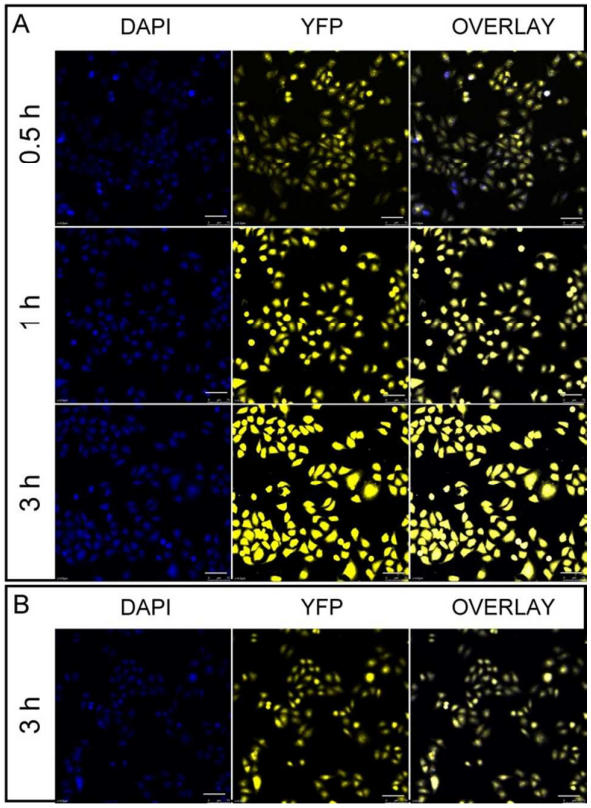

Fig. 4 Confocal laser scanning microscopy (CLSM) images of HeLa cells incubated with IZA (A) with magnet and (B) without magnet for different times. All the scale bars are 75 μm.

This assay uses oxidative stress sensitive dye DCFH-DA, a non-polar ROS-index probe which passively diffuses across cell membranes where it is hydrolyzed by intracellular esterase to the non-fluorescent polar derivative, DCFH. In the presence of ROS, DCFH is oxidized to DCF which is highly fluorescent and whose emission maximum can be monitored at 520 nm. As shown in Fig. 2 C and D, Hela cells incubated with Fe_3O_4/ZIF-8-Au_{25} under NIR irradiation present bright green fluorescence, while the sample incubated with Fe_3O_4/ZIF-8 shows no visible color, implying that Au_{25}-construct have the ability to product efficient ROS.

The cell viability of Fe_3O_4/ZIF-8-Au_{25} was evaluated through the viable cell ratio of L929 cells incubated with the sample with different concentrations (7.813, 15.625, 31.25, 62.5, 125, 250 and 500 μg/mL) for 24 h by standard methyl thiazolyl tetrazolium (MTT) assay (Fig. 2E). The bar chart obviously indicates that all the percentages of the viable cell are over 80%, even at a high concentration up to 500 μg/mL, suggesting no appreciable negative effect on the normal cells. To further ensure the safety of Fe_3O_4/ZIF-8-Au_{25} as an ideal candidate of drug carriers for biological applications, the as-synthesized sample should also be tested the biocompatibility with red blood cells. The hemolytic result and corresponding digital photographs are showed in Fig. 2F, which displays no obviously red color appears in each centrifuge tube of the sample with different concentration (from 7.813 to 1000 μg/mL), and the red solution in positive contrast tube is due to the haemoglobin dissolved in water. After keeping stable for 2 h at room temperature, the supernatants were measured by UV-*vis*. The percentages of hemolysis present a negligible enhancement with the increase of the concentration, and the highest hemolytic efficiency is less than 0.12%. It is indicative that Fe_3O_4/ZIF-8-Au_{25} has almost no side effect to red blood cells and no damage to blood, indicating the high *in vivo* biocompatibility of the sample.

The Fe_3O_4/ZIF-8-Au_{25} composite has a superparamagnetic response due to the successful encapsulation of Fe_3O_4 nanocrystals, which can act as a T_2 contrast agent for MR imaging, targeting agent and separating agent simultaneously. Fig. 3A shows the magnetic hysteresis loop of Fe_3O_4/ZIF-8-Au_{25}, as uncovered by field-dependent magnetization measurement at 300 K. The magnetization saturation value is 9.1 emu/g and the sample shows good dispersion with fast response to the external magnetic field. The result is desirable for various biomedical applications.

In the *In vitro* MRI experiment, T_2-weighted MR images of Fe_3O_4/ZIF-8-5mLAu_{25} using a 3T MR scanner reveal a clear concentration-dependent darkening effect, showing a high transverse relaxivity (r_2) of 35.49 $mM^{-1}{\cdot}s^{-1}$ (Fig. 3B). The corresponding amount of Fe_3O_4 nanoparticles encapsulated in the composite at different concentrations is examined by the ICP-MS. As shown, the MRI signal intensity of Fe_3O_4/ZIF-8-Au_{25} with different iron concentrations is negatively enhanced, the values of R_2 ($1/T_2$) are linearly increased. It is demonstrated that Fe_3O_4/ZIF-8-Au_{25} composite generates the magnetic resonance contrast on a transverse photon relaxation-time-weighted sequence to effectively shorten the T_2 relaxation time. Furthermore, *in vivo* T_2-weighted MRI was conducted *in situ* injection of Fe_3O_4/ZIF-8-Au_{25} into the tumor on a mouse (Fig. 3C). Comparing the images of tumor site before and after

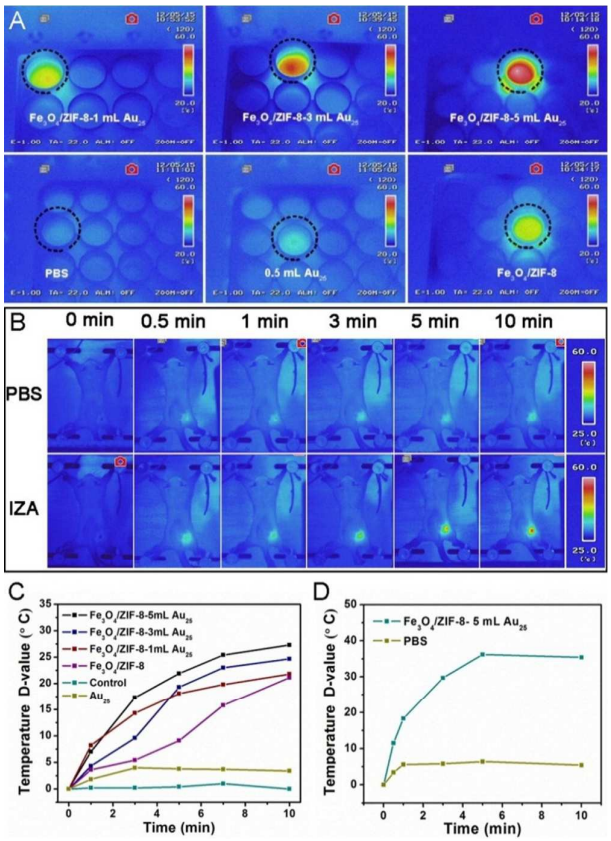

Fig. 5 *In vitro* and *in vivo* infrared thermal imaging properties and the corresponding temperature profiles. (A) The infrared thermal photograph of a 96-well HeLa cell-culture plate incubated with PBS, $Au_{25}(Capt)_{18}^-$ clusters, Fe_3O_4/ZIF-8 and Fe_3O_4/ZIF-8-Au_{25} after 808 nm NIR irradiation (0.5 W/cm^2) for 5 min; (B) the infrared thermal images of a tumor-bearing mouse after injection of Fe_3O_4/ZIF-8 Au_{25}-5mL as a function of the irradiation time irradiated by 808 nm NIR light (0.5 W/cm^2); (C, D) the corresponding temperature profiles of (A) and (B).

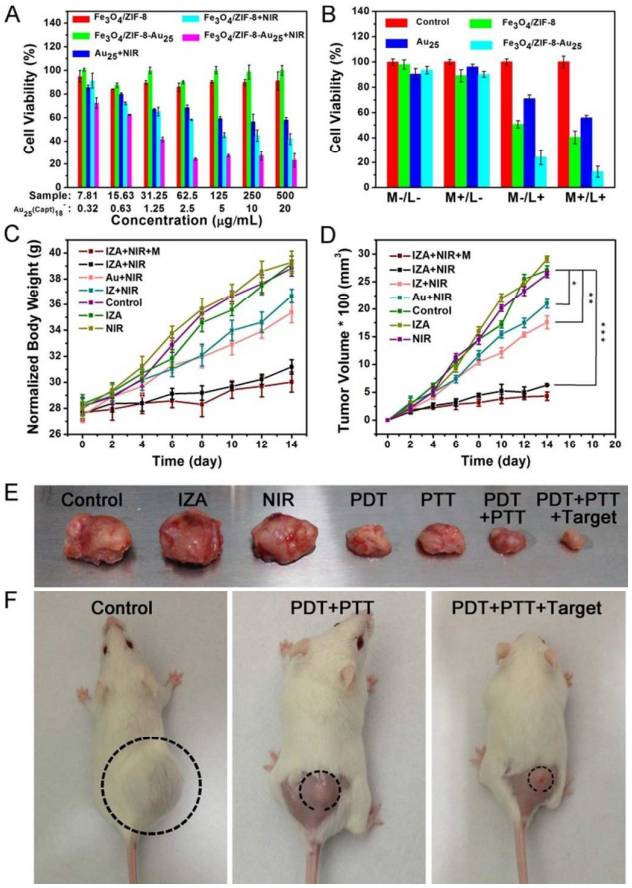

Fig. 6 *In vitro* and *in vivo* anti-cancer properties. (A, B) *In vitro* viability of HeLa cells incubated for 24 h with IZA, IZ, and $Au_{25}(Capt)_{18}^-$ clusters at varied concentration with and without two types of stimuli (NIR-laser irradiation (L) and magnet remote control (M)); (C) the body weight and (D) relative tumor volume of H22 tumor in different groups *versus* the treatment time. *p < 0.05, ***p < 0.01 (n = 5); (E) representative photographs of the tumor tissues excised from tumor-bearing mice treated with normal saline, pure NIR laser, pure IZ, pure $Au_{25}(Capt)_{18}^-$ clusters with NIR-laser irradiation, IZA with or without NIR-laser irradiation and IZA with two types of stimuli (NIR-laser irradiation (L) and magnet remote control (M)) on the 14th day, (F) the digital photographs of representative mice on the 14th day.

injection, a apparent signal attenuation effect on the tumor site is observed after injection, which demonstrates the capability of MR contrast enhancement effect of Fe_3O_4 doped nanocomposite.

To determine the accumulation and subcellular localization of Fe_3O_4/ZIF-8-Au_{25} composite in HeLa cells, we performed the uptake study and CLSM observation *in vitro*, as shown in Fig. 4. In general, nanoparticles enter cells via endocytosis and finally fuse with lysosome. Lysosome is subcellular organelle which is consisted of many kinds of enzymes and also responsible for digesting material consuming from the cell surface presented via endocytosis. HeLa cells are incubated with Fe_3O_4/ZIF-8-Au_{25} for different time with and without a magnetic field. The images from left to right successively show cell nuclei stained by DAPI which emits blue fluorescence for mark the nuclei, yellow fluorescence of $Au_{25}(Capt)_{18}^-$ clusters in the carrier in cells, and overlays of above two images correspondingly. It is clear that the stronger yellow fluorescence emission of $Au_{25}(Capt)_{18}^-$ clusters is observed in both cytoplasm and cell nucleus, suggesting that more nanoparticles are phagocytized with the increase of the incubation time. The results reveal that Fe_3O_4/ZIF-8-Au_{25} nanoparticles can be effectively taken up by tumor cells. To further verify the enhanced cell uptake of nanoparticles induced by external magnetic stimulation, we have also done a contrast experiment in the absence of magnetic field. Remarkably reduced materials uptake is found (Fig. 4B) compared with those assisted with external magnetic field. A digital photograph showing the experimental set-up to the cells after magnetic targeted uptake assay is given in Fig. S5. The magnet is placed close to the cell culture dish and the sample is adsorbed to the surrounding of magnet.

***In vitro* and *in vivo* cytotoxicity assay.** Another important property of Fe_3O_4/ZIF-8-Au_{25} composite is their photothermal effect due to the presence of Fe_3O_4 nanoparticles and $Au_{25}(Capt)_{18}^-$ clusters. To verify our hypothesis, we undertook infrared thermal imaging test *in vitro* using HeLa cells incubated with PBS, $Au_{25}(Capt)_{18}^-$ clusters, Fe_3O_4/ZIF-8 and

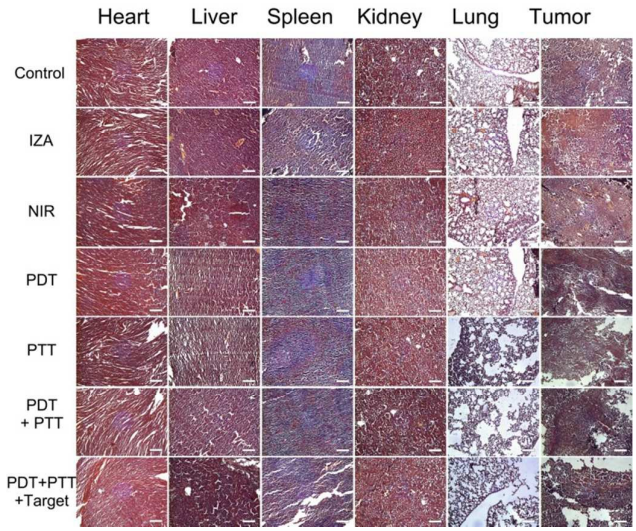

Fig. 8 Representative H&E stained histological images of the superficial regions of tumor, heart, liver, spleen, lung and kidney slices. All the scale bars are 75 μm.

Fe_3O_4/ZIF-8-Au_{25} under irradition of 808 nm laser (0.5 W/cm^2) for 5 min, and the result is given in Fig. 5. As expected, the wells incubated with Fe_3O_4/ZIF-8 and Fe_3O_4/ZIF-8-Au_{25} particles show high contrast infrared thermal images and obvious temperature elevation (Fig. 5A). However, no visible temperature increase is found in the wells incubated with $Au_{25}(SR)_{18}^-$ clusters only. Importantly, the temperature of HeLa cells incubated with Fe_3O_4/ZIF-8-5mLAu_{25} is rapidly increased to about 60 °C only after 10 min irradiation. Such temperature is high enough to kill HeLa cells, which is higher than cell death temperature (40-60 °C).[50] We further investigated the photothermal effect *in vivo*. Inspiringly, infrared thermal images with high contrast can be also acquired under a low-power density laser irradiation (0.5 W/cm^2), as showed in Fig. 5B. Meanwhile, the temperature profiles of HeLa cell supernatant and a tumor-bearing mouse treated with Fe_3O_4/ZIF-8-5mLAu_{25} as a function of the irradiation time with 808 nm irradiation (0.5 W/cm^2) *in vitro*/*in vivo* are given in Fig.4C and D, which is well consistent with the aforementioned results.

To investigate the tumor inhibition efficacy of the sample, the *in vitro* cytotoxicity to HeLa cells was evaluated by means of a MTT assay through altering two variables of concentration and external condition. In Fig. 6, the viability of cells treated with Fe_3O_4/ZIF-8-Au_{25}, Fe_3O_4/ZIF-8 and $Au_{25}(Capt)_{18}^-$ clusters without other external conditions at the concentration of 500 μg/mL doesn't show significant downward trend (Fig. 6A).

Even at the concentration of 500 mg/mL, the cell viability still remains above 80%, indicating that the sample has good cytocompatibility within the concentration range, which is essential for their biological application. Meanwhile, different degrees of decreases of cell viability are observed after the cells were incubated with Fe_3O_4/ZIF-8-Au_{25}, Fe_3O_4/ZIF-8 and $Au_{25}(Capt)_{18}^-$ under 808 nm NIR irradiation at various concentrations (7.813-500 mg/mL) for 24 h. In addition, the result in Fig. 6B further manifests the obvious inhibition efficacy of the sample after laser irradiation due to the combined photothermal and photodynamic killing effects induced by the 808 nm laser light and enhanced cell uptake of nanoparticles stimulated by the external magnetic field. It is worth noting that cells incubated with Fe_3O_4/ZIF-8-Au_{25} after two types of stimuli (the NIR light and magnet remote control) are remarkably killed with less than 15% cell viability. The result is also verified by the CLSM images of HeLa cells dyed with calcein AM and PI. Moreover, we added a cytotoxicity experiment of Hepal-6 cells which is the corresponding *in vitro* cells of the following H22 (murine hepatocarcinoma) of the mice, as shown in Fig. S6. It is apparent that the cytotoxicity result on Hepal-6 cells is consistent with the result on HeLa cells. Good cytocompatibility and excellent inhibition efficacy of Fe_3O_4/ZIF-8-Au_{25} responsive to external stimuli imply that the tested NPs can serve as bio-probe and contrast agent in biomedical application.

To further determine whether remarkable anticancer ability of the above tested nanoparticles are also obtained *in vivo*, a series of contrast experiments were employed, and the results are given in Fig. 6C-F. Body weight is an important parameter to evaluate the systemic toxicity of the material to the body. In our experiment, the body weights of all groups are obviously increased with prolonged time, implying no obvious side effect on our tested groups (Fig. 6C). Moreover, the volume growth of tumors treated with pure 808 nm laser or only IZA shows no noticeable difference from those treated with saline. This can be attributed to the fact that the NIR light and IZA composite is safe for the tissue and short interval irradiation can avoid overheating by the NIR light. More importantly, for tumor-bearing mice treated only by PDT (pure $Au_{25}(Capt)_{18}^-$ clusters under NIR) and PTT (IZ under NIR), the tumor growth inhibition efficacy is much lower than that treated by the combined PDT and PTT (IZA under NIR). In stark contrast, the representative photographs of tumor tissues excised from tumor-bearing mice and representative mice with tumors on the 14th day (Fig. 6E, F) also present that the tumor size under "PDT+PTT" treatments is evidently smaller than those only treated with PDT or PTT alone. Furthermore, most tumor tissue cells under "PDT+PTT+Magnetic" are destroyed compared to the others, which can directly suggest the high inhibition effect.

To reveal any potential toxic effects of IZA to the treated mice, we carried out blood biochemistry. The blood levels of liver function markers, including alanine aminotransferase (ALT), aspartate aminotransferase (AST), alkaline phosphatase (ALP), and the ratio of albumin and globulin (A/G) of IZA treated mice, were all consistent with those of the control healthy mice, suggesting that no obvious hepatic toxicity was induced by IZA treatment. The blood urea level, which was an indicator of kidney functions, was also normal for treated mice. We selected the following important hematology markers for the haematological assessment: white blood cells (WBC), red blood cells (RBC), hemoglobin (HGB), mean corpuscular volume (MCV), mean corpuscular haemoglobin (MCH), mean corpuscular hemoglobin concentration (MCHC), platelets (PLT), and hematocrit (HCT). All of the above parameters in the IZA-treated mice appear to be normal

compared with the control groups and are in agreement with the reference normal ranges.[73]

In addition, the hematoxylin and eosin (H&E) staining images of tumor tissues after 14 day treatment are presented in Fig. 8. Neither obvious apoptosis nor noticeable pathological changes can be detected in the heart, lung, kidney, liver, spleen and tumor cells retain their normal morphology with distinctive membrane and nuclear structures in the groups receiving both IZA injection and NIR laser irradiation, which indicates no significant acute toxicity of our theranostic agents. However, the tumor cells are destroyed to various degrees in the other therapeutic groups. These results are in good agreement with the tumor growth results, further confirming the superior therapeutic efficacy of the combined therapies of noninvasive PTT and PDT.

Conclusions

In summary, inorganic-organic Fe_3O_4/ZIF-8-Au_{25} nanocomposite has been successfully designed by a facile route for multimodal cancer therapy. Upon 808 nm NIR light irradiation, the attached $Au_{25}(Capt)_{18}^-$ clusters can generate hyperthermia to produce a unique photothermal therapy modality, efficient singlet oxygen can also be produced for PDT. Meanwhile, the encapsulated Fe_3O_4 nanocrystals can also be served as a PTT agent. The combined PTT and PDT are responsible for the high inhibition efficacy of tumor cells. Considering the MRI property and the magnet responsive cytotoxicity, it is conceivable that this composite is a promising candidate in anti-tumor therapy.

Experimental section

Materials and synthesis. All chemical reagents were used as received without further purification containing concentrated ammonia aqueous solution (25 wt.%), tetrachloroauric (III) acid ($HAuCl_4 \cdot 3H_2O$, 99.99%), sodium borohydride ($NaBH_4$, 99.99%), 3,3′-diaminobenzidine (DAB > 99%), methanol, phosphate buffered saline (PBS), and anhydrous ethanol (from Beijing Chem. Co. Ltd. $FeCl_3$ (97%), $Zn(NO_3)_2 \cdot 6H_2O$ (99%), MeIM (98%), PAA (M_w = 1800), and diethylene glycol (DEG, 99%) were purchased from Aladdin Co. Ltd. aminopropyltrimethoxysilane (APTES), 3-4,5-dimethylthiazol-2-yl-2,5-diphenyl tetrazolium bromide (MTT), dimethyl sulfoxide (DMSO), 4′,6-diamidino-2-phenylindole (DAPI), calcein AM and propidium iodide (PI), captopril and tetraoctylammonium bromide (TOAB, > 98%) were purchased from Sigma-Aldrich Co. (USA).

Synthesis of PAA-grafted Fe_3O_4 nanocrystals. PAA-grafted Fe_3O_4 nanocrystals were synthesized by a reported route.[71,72] The NaOH/DEG mixed solution was firstly prepared. NaOH (2.5 mmol/mL) was dissolved in DEG (8 mL) and then this solution was raised to 120 °C and heated for 1 h under nitrogen, the cooled and kept at 70 °C. Secondly, PAA (0.576 g) and $FeCl_3$ (1.08 g) were added into 30 mL of DEG to form a transparent solution. After that, the mixture was heated to 220 °C in N_2 under vigorous stirring until the solution changes to light yellow. NaOH/DEG solution (8 mL) was quickly injected into above solution under vigorous stirring. After keeping at 220 °C for 2 h, the solution was cooled to room temperature. The final product was washed with deionized water and ethanol several times and then dispersed in 10 mL of deionized water.

Synthesis of Fe_3O_4/ZIF-8 nanoparticles. Briefly, an aqueous solution of MeIM (3.45 mol/L, 20 mL) was first mixed with the aforementioned aqueous solution of Fe_3O_4 nanocrystals (2.5 mL) by sonication, and stirred at a speed of 400 rpm at room temperature. Then the aqueous solution of $Zn(NO_3)_2$ (0.35 mol/L, 4 mL) was loaded in a syringe and gradually added to the above solution over 20 min by means of a syringe pump to produce Fe_3O_4/ZIF-8 particles. After the addition of $Zn(NO_3)_2$, the products were separated by centrifugation, washed with deionized water twice, and dried at 300 °C under the protection of N_2 flow for 2 h.

Synthesis of $Au_{25}(Capt)_{18}^-$ clusters. Typically, 78.7 mg of $HAuCl_4 \cdot 3H_2O$ and 12.8 mg (0.23 mmol) of TOAB were dissolved in 10 mL of methanol and vigorously stirred for 20 min. After that, 217.2 mg (1 mmol) of captopril was dissolved in 5 mL of methanol and rapidly injected in the solution, and further stirred for 30 min. Then, 75.6 mg (2 mmol) of $NaBH_4$ was dissolved in 5 mL of ice-cold water and rapidly added with vigorous stirring. After the reaction for 8 h, the solution was centrifuged to remove insoluble Au(I) polymer. The supernatant was recovered and treated by rotary evaporation and then obtained by adding ethanol. The powder was extracted several times with little amounts of methanol, and then the clusters were obtained and dried in vacuum.

Synthesis of $Au_{25}(Capt)_{18}^-$ attached Fe_3O_4/ZIF-8. Firstly, PAA was functionalized on Fe_3O_4/ZIF-8 by a ligand exchange approach. 0.1 g of as-prepared Fe_3O_4/ZIF-8 nanoparticles was dispersed in 20 mL of deionized water. 0.15 mL of APTES was added into the solution and heated at 45 °C for 8 h with stirring, then centrifugated, washed with ethanol and finally dried at 60 °C. The obtained sample was dispersed in 20 mL of ethanol containing 5 mL of as-prepared $Au_{25}(Capt)_{18}^-$ clusters with continuous stirring for 4 h at 60 °C in the dark. The obtained product was denoted as Fe_3O_4/ZIF-8-Au_{25} (IZA).

Characterization. Powder X-ray diffraction (XRD) patterns were recorded on a Rigaku D/max TTR-III diffractometer at a scanning rate of 15°/min from 10° to 80°, using graphite monochromatized Cu Kα radiation (λ = 0.15405 nm). Transmission electron microscopy (TEM) and high-resolution transmission electron microscopy (HRTEM) images were obtained on FEI Tecnai G^2 S-Twin. N_2 adsorption/desorption isotherms were measured on a Micromeritics ASAP Tristar II 3020 apparatus. Pore size distribution was determined by the Barrete-Jonere-Halenda (BJH) method. UV-*vis* spectra were recorded on a UV-1601 spectrophotometer.

***In vitro* and *in vivo* T_2-weighted MR imaging.** The *in vitro* MR imaging properties were examined on a 3 T MRI magnet (Shanghai Niumai Corporation Ration NM120-Analyst). Briefly, IZA nanoparticles were dispersed in water with various Fe_3O_4 concentrations (determined by ICP-MS). T_2 value was acquired using an inversion recovery sequence. T_2 measurement was performed using a nonlinear fit to change in the mean signal intensity within each well as a function of repetition time (TR) with a Huantong 1.5 T MR scanner. Finally, the r_1 relaxivity

values were calculated by the curve fitting of $1/T_2$ relaxation time (s^{-1}) *versus* the Fe_3O_4 concentration (mM). MR imaging of mice was accomplished with the same 3 T clinical MR scanner equipped with a special coil used for small-animal imaging.

Detection of singlet oxygen. Here, we used water-soluble DAB as probe for detecting $^1O_2$. Typically, a stock solution of DAB in DMF (10 mM) was prepared and was then added into 2 mL of IZA solution to achieve final IZA and DAB concentrations of 40–85 and 500 μM, respectively. The solution was then purged with air for 10 min in the dark. The solutions were irradiated with 650 nm (0.5 W/cm^2), or 808 nm laser (0.5 W/cm^2) for 10 min, or then irradiated with a 650 nm laser (0.5 W/cm^2) for different time. The adsorption spectra were measured after different period of laser irradiation.

***In vitro* cell viability.** Typically, to let monolayer cells attach the wells, we cultivated L929 fibroblast cells (7000-8000/well) a 96-well plate, and incubated at 37 °C for 24 h in 5% CO_2. After that, the tested samples were diluted into respective concentration of 7.813, 15.625, 31.25, 62.5, 125, 250, and 500 μg/mL, and then the solutions were added into the wells and further incubated for 24 h. For blank control, 8 wells were left with culture only. Then, 0.02 mL of as-fabricated MTT solution was added into each well and further incubated for 4 h at 37 °C. At last, 150 mL of DMSO was added into every well and stand on a shaking table for 5 min at 150 rpm so as to completely blend the solvent and formazan. The absorbance spectra were measured on a micro-plate reader at 490 nm. The optical density that received no drug was considered as 100% growth.

Hemolysis assay. The EDTA.K2 stabilized human blood was firstly washed by 1% normal saline, then centrifugated several times till the supernatant was transparent, then red blood cells were obtained. After that, the blood cells were diluted to 1/10 with PBS solution (pH = 7.4). 0.3 mL of diluted cells suspension was mixed with deionized water (1.2 mL), PBS (1.2 mL), and 1.2 mL of DSHSs-Cu_xS sample suspensions with concentration of 15.625, 31.25, 62.5, 125, 250, 500, and 1000 μg/mL, respectively. After shaken and kept for 2 h, the mixtures were centrifuged and the absorbance spectra of the supernatants were recorded on a UV-*vis* spectroscopy. The hemolytic percentage was calculated by the equation: *Hemolysis* % = (A_{sample} - $A_{control(-)}$) / ($A_{control(+)}$ - $A_{control(-)}$), where A is the absorbance of UV-*vis* spectra.

Blood biochemistry assay. Blood biochemistry and hematology data of female mice were treated with IZA at the dose of 2 mg/mL at 20 days. Age-matching untreated mice were sacrificed at 20 days as controls group. An approximately 0.8 mL portion of blood from each mouse was collected for the blood chemistry test and complete blood panel analysis.

Cellular uptake. Cellular uptake by HeLa cancer cells was measured on a confocal laser scanning microscope (CLSM). Typically, HeLa cells (5 × 10^4/well) were firstly seeded in 6-well culture plates and grown for 12 h before uptake study, then incubated with as-prepared IZA (2 mL, 500 μg/mL) with and without a magnet at 37 °C for different time (0.5 h, 1 h and 3 h). At different time points, the cells were rinsed with PBS three times. After that, the cells were fixed with 2.5% formaldehyde (1 mL/well) at 37 °C for 10 min and further rinsed with PBS three times. So as to carry out nucleus labeling, the nuclei were stained with DAPI solution (20 μg/mL in PBS, 1 mL/well) for 10 min, and the cells were rinsed with PBS three times again. The coverslips were placed on a glass microscope slide, and the samples were measured on Leica TCS SP8.

***In vitro* cytotoxicity**. The cytotoxicity of IZA is detected similar to the viability MTT assay by incubation of HeLa cancer cells instead of L929 fibroblast cells. The difference is that the HeLa cells viabilities *in vitro* incubated for 24 h with control, $Au_{25}(Capt)_{18}^-$, IZ, IZA with and without NIR irradiation (pump power of 0.5 W/cm^2) or magnet with different concentrations.

Dye experiment. HeLa cells were seeded in a 6-well culture plate and grown overnight, then 2 mL of 0.5 mg/mL samples was added. After incubation for 4 h, the cells were irradiated by the 808 nm light (0.5 mW/cm^2) for 10 min. After culturing for 12 h, dead and live cells were stained with propidium iodide (PI, 5 mM) and calcein AM (2 mM), and visualized using CLSM (Leica TCS SP8).

Intracellular ROS assay. Intracellular ROS assay by HeLa cancer cells was measured on a confocal laser scanning microscope (CLSM). Typically, HeLa cells (5 × 10^4/well) were firstly seeded in 6-well culture plates and grown for 12 h before Intracellular ROS assay study, then incubated with as-prepared IZA (2 mL, 500 μg/mL) in the dark for 24 h at 37°C. During that time, HeLa cells were exposured under 808 nm light (0.5 mW/cm^2) for 10 min. After that, PBS was then added followed by wash three times. After removal of the supernatant, the cell pellet was re-added in 1 ml carboxy-DCFH-DA. Finally, the cell pellet was re-rinsed by PBS and the coverslips were placed on a glass microscope slide, and the samples were measured on Leica TCS SP8.

***In vivo* toxicity.** Female Balb/c (25-35 g) mice were purchased from Harbin Veterinary Research Institute, Chinese Academy of Agricultural Sciences (Harbin, China). All the mice experiments were performed in accordance with the criterions of The National Regulation of China for Care and Use of Laboratory Animals, and all animal procedures were approved by the University Animal Care and Use Committee. Typically, the tumors were generated in the right back of each mouse by subcutaneous injection of H22 cells (murine hepatocarcinoma cell lines). After one week, the tumors sizes grew to 6-10 mm with the body weight reached 25-30 g. The tumor-bearing mice were randomly divided into seven groups (n = 5, each group) and intratumorally injected with normal saline, IZ, IZ with NIR irradiation, pure $Au_{25}(Capt)_{18}^-$ clusters, IZA, IZA with NIR irradiation or IZA with two external stimulus of NIR irradiation and magnet, respectively. The first group was regarded as blank control group without injecting any material. The amount of injected material is 0.1 mL/mice every two days, and the quantity of pure $Au_{25}(Capt)_{18}^-$ clusters is in accordance with the loading of IZA detected by ICP-MS. For the NIR irradiation process, we irradiated the tumor site with 808 nm laser for 10 min after injecting different materials for 1 h. The tumor sizes and body weights were recorded every two days after treatment.

Histological examination. Histology measurement was performed after 14 days treatment. The typical heart, liver, spleen, kidney, lung, and tumor tissues of the mice were isolated. After that, the organs were dehydrated using buffered formalin, ethanol with different concentrations, and xylene. After that, they were embedded in liquid paraffin. The sliced organs and tumor tissues (3-5 mm) were stained with Hematoxylin and Eosin (H&E) and examined on Leica TCS SP8.

Acknowledgements

Financial support from National Natural Science Foundation of China (NSFC 21271053, 21401032, 51472058), NCET in University (NCET-12-0622), Natural Science Foundation of Heilongjiang Province (B201403), Heilongjiang Postdoctoral Fund (LBH-Z14052), General Financial Grant from the China Postdoctoral Science Foundation (2014M560248), Special Financial Grant from the China Postdoctoral Science Foundation (2015T80321), and Fundamental Research Funds for the Central Universities of China are greatly acknowledged.

Notes and references

1 Z. Zhang, Y. Chen, X. Xu, J. Zhang, G. Xiang, W. He and X. Wang, *Angew. Chem. Int. Edit.*, 2014, **53**, 429-433.
2 A. J. Howarth, M. J. Katz, T. C. Wang, A. E. Platero-Prats, K. W. Chapman, J. T. Hupp and O. K. Farha, *J. Am. Chem. Soc.*, 2015, **137**, 7488-7494.
3 X. Zhu, B. Li, J. Yang, Y. Li, W. Zhao, J. Shi and J. Gu, *ACS Appl. Mater. Inter.*, 2015, **7**, 223-231.
4 M. D. Allendorf, C. A. Bauer, R. K. Bhakta and R. J. T. Houk, *Chem. Soc. Rev.*, 2009, **38**, 1330-1352.
5 V. Stavila, A. A. Talin and M. D. Allendorf, *Chem. Soc. Rev.*, 2014, **43**, 5994-6010.
6 Y. Liu, S. Zhou, D. Tu, Z. Chen, M. Huang, H. Zhu, E. Ma and X. Chen, *J. Am. Chem. Soc.*, 2012, **134**, 15083-15090.
7 7.J. Yang, Y. Dai, X. Zhu, Z. Wang, Y. Li, Q. Zhuang, J. Shi and J. Gu, *J. Mater. Chem. A*, 2015, **3**, 7445-7452.
8 M. D. Allendorf, R. J. T. Houk, L. Andruszkiewicz, A. A. Talin, J. Pikarsky, A. Choudhury, K. A. Gall and P. J. Hesketh, *J. Am. Chem. Soc.*, 2008, **130**, 14404-14405.
9 J. Della Rocca, D. Liu and W. Lin, *Acc. Chem. Res.* , 2011, **44**, 957-968.
10 S. T. Meek, J. A. Greathouse and M. D. Allendorf, *Adv. Mater.*, 2011, **23**, 249-267.
11 D. Cunha, M. Ben Yahia, S. Hall, S. R. Miller, H. Chevreau, E. Elkaim, G. Maurin, P. Horcajada and C. Serre, *Chem. Mater.*, 2013, **25**, 2767-2776.
12 L.-L. Tan, H. Li, Y. Zhou, Y. Zhang, X. Feng, B. Wang and Y.-W. Yang, *Small* 2015, **11**, 3807-3813.
13 J. Lee, O. K. Farha, J. Roberts, K. A. Scheidt, S. T. Nguyen and J. T. Hupp, *Chem. Soc. Rev.*, 2009, **38**, 1450-1459.
14 A. Corma, H. Garcia and F. X. L. I. Llabres i Xamena, *Chem. Rev.*, 2010, **110**, 4606-4655.
15 D. Wang, T. Xie, Q. Peng and Y. Li, *J. Am. Chem. Soc.*, 2008, **130**, 4016-4022.
16 H. Guo, Y. Zhu, S. Wang, S. Su, L. Zhou and H. Zhang, *Chem. Mater.*, 2012, **24**, 444-450.
17 K. R. Deng, Z. Y. Hou, X. J. Li, C. X. Li, Y. X. Zhang, X. R. Deng, Z. Y. Cheng and J. Lin, *Sci. Rep.*, 2015, **5**, 7.
18 A. C. McKinlay, R. E. Morris, P. Horcajada, G. Ferey, R. Gref, P. Couvreur and C. Serre, *Angew. Chem. Int. Edit.*, 2010, **49**, 6260-6266.
19 P. Horcajada, C. Serre, M. Vallet-Regi, M. Sebban, F. Taulelle and G. Ferey, *Angew. Chem. Int. Edit.*, 2006, **45**, 5974-5978.
20 J. Zhuang, C.-H. Kuo, L.-Y. Chou, D.-Y. Liu, E. Weerapana and C.-K. Tsung, *ACS Nano*, 2014, **8**, 2812-2819.
21 Y.-n. Wu, M. Zhou, S. Li, Z. Li, J. Li, A. Wu, G. Li, F. Li and X. Guan, *Small*, 2014, **10**, 2927-2936.
22 I. B. Vasconcelos, T. G. da Silva, G. C. G. Militao, T. A. Soares, N. M. Rodrigues, M. O. Rodrigues, N. B. da Costa, Jr., R. O. Freire and S. A. Junior, *RSC. Adv.*, 2012, **2**, 9437-9442.
23 L. Cheng, K. Yang, Y. Li, J. Chen, C. Wang, M. Shao, S. T. Lee and Z. Liu, *Angew. Chem. Int. Edit.*, 2011, **50**, 7385-7390.
24 W. Li, J. Wang, J. Ren and X. Qu, *J. Am. Chem. Soc.*, 2014, **136**, 2248-2251.
25 Z. Cheng, Y. Dai, X. Kang, C. Li, S. Huang, H. Lian, Z. Hou, P. Ma and J. Lin, *Biomaterials*, 2014, **35**, 6359-6368.
26 L. Cheng, K. Yang, Y. Li, X. Zeng, M. Shao, S.-T. Lee and Z. Liu, *Biomaterials*, 2012, **33**, 2215-2222.
27 L. J. Zhao, H. J. Zhang, Y. Xing, S. Y. Song, S. Y. Yu, W. D. Shi, X. M. Guo, H. H. Yang, Y. Q. Le and F. Cao, *Chem. Mater.*, 2008, **20**, 198-204.
28 M. Chu, Y. Shao, J. Peng, X. Dai, H. Li, Q. Wu and D. Shi, *Biomaterials*, 2013, **34**, 4078-4088.
29 W. Wang, C. Fang, X. Wang, Y. Chen, Y. Wang, W. Feng, C. Yan, M. Zhao and S. Peng, *Nanoscale*, 2013, **5**, 6249-6253.
30 S. Gai, C. Li, P. Yang and J. Lin, *Chem. Rev.*, 2014, **114**, 2343-2389.
31 M.-K. Tsang, G. Bai and J. Hao, *Chem. Soc. Rev.*, 2015, **44**, 1585-1607.
32 T. Zhang, C.-F. Chan, J. Hao, G.-L. Law, W.-K. Wong and K.-L. Wong, *RSC. Adv.*, 2013, **3**, 382-385.
33 X. D. Zhang, J. Chen, Z. T. Luo, D. Wu, X. Shen, S. S. Song, Y. M. Sun, P. X. Liu, J. Zhao, S. D. Huo, S. J. Fan, F. Y. Fan, X. J. Liang and J. P. Xie, *Adv. Healthc. Mater.*, 2014, **3**, 133-141.
34 L. V. Nair, D. S. Philips, R. S. Jayasree and A. Ajayaghosh, *Small*, 2013, **9**, 2673-2677.
35 N. Niu, F. He, P. a. Ma, S. Gai, G. Yang, F. Qu, Y. Wang, J. Xu and P. Yang, *ACS Appl. Mater. Inter.*, 2014, **6**, 3250-3262.
36 G. Yang, R. Lv, S. Gai, Y. Dai, F. He and P. Yang, *Inorg. Chem.*, 2014, **53**, 10917-10927.
37 Y. Wang, S. Song, J. Liu, D. Liu and H. Zhang, *Angew. Chem. Int. Edit.*, 2015, **54**, 536-540.
38 X. Zhang, P. Yang, Y. Dai, P. a. Ma, X. Li, Z. Cheng, Z. Hou, X. Kang, C. Li and J. Lin, *Adv. Funct. Mater.*, 2013, **23**, 4067-4078.
39 R. Bardhan, W. Chen, C. Perez-Torres, M. Bartels, R. M. Huschka, L. L. Zhao, E. Morosan, R. G. Pautler, A. Joshi and N. J. Halas, *Adv. Funct. Mater.*, 2009, **19**, 3901-3909.
40 H. Liu, T. Liu, X. Wu, L. Li, L. Tan, D. Chen and F. Tang, *Adv. Mater.*, 2012, **24**, 755-761.
41 Z. Zhang, L. Wang, J. Wang, X. Jiang, X. Li, Z. Hu, Y. Ji, X. Wu and C. Chen, *Adv. Mater.*, 2012, **24**, 1418-1423.
42 Y. Xia, W. Li, C. M. Cobley, J. Chen, X. Xia, Q. Zhang, M. Yang, E. C. Cho and P. K. Brown, *Acc. Chem. Res.* , 2011, **44**, 914-924.
43 J. Chen, M. Yang, Q. Zhang, E. C. Cho, C. M. Cobley, C. Kim, C. Glaus, L. V. Wang, M. J. Welch and Y. Xia, *Adv. Funct. Mater.*, 2010, **20**, 3684-3694.
44 Z. Lin, Y. Liu, X. Ma, S. Hu, J. Zhang, Q. Wu, W. Ye, S. Zhu, D. Yang, D. Qu and J. Jiang, *Sci. Rep.*, 2015, **5**.

45 K. Yang, L. Hu, X. Ma, S. Ye, L. Cheng, X. Shi, C. Li, Y. Li and Z. Liu, *Adv. Mater.*, 2012, **24**, 1868-1872.
46 Z. Zhao, S. Shi, Y. Huang, S. Tang and X. Chen, *ACS Appl. Mater. Inter.*, 2014, **6**, 8878-8885.
47 Y. Zhao, W. Song, D. Wang, H. Ran, R. Wang, Y. Yao, Z. Wang, Y. Zheng and P. Li, *ACS Appl. Mater. Inter.*, 2015, **7**, 14231-14242.
48 Z. Zhou, Y. Sun, J. Shen, J. Wei, C. Yu, B. Kong, W. Liu, H. Yang, S. Yang and W. Wang, *Biomaterials*, 2014, **35**, 7470-7478.
49 S. Shen, S. Wang, R. Zheng, X. Zhu, X. Jiang, D. Fu and W. Yang, *Biomaterials*, 2015, **39**, 67-74.
50 Q. Tian, J. Hu, Y. Zhu, R. Zou, Z. Chen, S. Yang, R. Li, Q. Su, Y. Han and X. Liu, *J. Am. Chem. Soc.*, 2013, **135**, 8571-8577.
51 R. Lv, P. Yang, F. He, S. Gai, G. Yang and J. Lin, *Chem. Mater.*, 2015, **27**, 483-496.
52 C. Wang, H. Xu, C. Liang, Y. Liu, Z. Li, G. Yang, H. Cheng, Y. Li and Z. Liu, *ACS Nano*, 2013, **7**, 6782-6795.
53 W. Feng, X. Zhou, W. Nie, L. Chen, K. Qiu, Y. Zhang and C. He, *ACS Appl. Mater. Inter.*, 2015, **7**, 4354-4367.
54 J. Zhou, Z. Lu, X. Zhu, X. Wang, Y. Liao, Z. Ma and F. Li, *Biomaterials*, 2013, **34**, 9584-9592.
55 M. Guan, H. Dong, J. Ge, D. Chen, L. Sun, S. Li, C. Wang, C. Yan, P. Wang and C. Shu, *Npg Asia Mater.*, 2015, **7**.
56 J. Lin, S. Wang, P. Huang, Z. Wang, S. Chen, G. Niu, W. Li, J. He, D. Cui, G. Lu, X. Chen and Z. Nie, *ACS Nano*, 2013, **7**, 5320-5329.
57 Y. Wang, H. Wang, D. Liu, S. Song, X. Wang and H. Zhang, *Biomaterials*, 2013, **34**, 7715-7724.
58 B. Tian, C. Wang, S. Zhang, L. Feng and Z. Liu, *ACS Nano*, 2011, **5**, 7000-7009.
59 J. Peng, L. Zhao, X. Zhu, Y. Sun, W. Feng, Y. Gao, L. Wang and F. Li, *Biomaterials*, 2013, **34**, 7905-7912.
60 Z. Hou, Y. Zhang, K. Deng, Y. Chen, X. Li, X. Deng, Z. Cheng, H. Lian, C. Li and J. Lin, *ACS Nano*, 2015, **9**, 2584-2599.
61 L. M. Pan, J. A. Liu and J. L. Shi, *Adv. Funct. Mater.*, 2014, **24**, 7318-7327.
62 S. Lu, D. T. Tu, P. Hu, J. Xu, R. F. Li, M. Wang, Z. Chen, M. D. Huang and X. Y. Chen, *Angew. Chem. Int. Edit.*, 2015, **54**, 7915-7919.
63 L. V. Nair, S. S. Nazeer, R. S. Jayasree and A. Ajayaghosh, *Acs Nano*, 2015, **9**, 5825-5832.
64 R. Liang, L. Ma, L. Zhang, C. Li, W. Liu, M. Wei, D. Yan, D. G. Evans and X. Duan, *Chem. Commun.* , 2014, **50**, 14983-14986.
65 R. Lv, P. Yang, F. He, S. Gai, C. Li, Y. Dai, G. Yang and J. Lin, *ACS Nano*, 2015, **9**, 1630-1647.
66 Z. Li, C. Wang, L. Cheng, H. Gong, S. Yin, Q. Gong, Y. Li and Z. Liu, *Biomaterials*, 2013, **34**, 9160-9170.
67 P. Huang, J. Lin, X. Wang, Z. Wang, C. Zhang, M. He, K. Wang, F. Chen, Z. Li, G. Shen, D. Cui and X. Chen, *Adv. Mater.*, 2012, **24**, 5104-5110.
68 H. Kawasaki, S. Kumar, G. Li, C. Zeng, D. R. Kauffman, J. Yoshimoto, Y. Iwasaki and R. Jin, *Chem. Mater.*, 2014, **26**, 2777-2788.
69 S. Kumar and R. Jin, *Nanoscale*, 2012, **4**, 4222-4227.
70 F. He, G. Yang, P. Yang, Y. Yu, R. Lv, C. Li, Y. Dai, S. Gai and J. Lin, *Adv. Funct. Mater.*, 2015, **25**, 3966-3976.
71 F. Pang, M. He and J. Ge, *Chem. Eur. J.*, 2015, **21**, 6879-6887.
72 J. Ge, Y. Hu, M. Biasini, W. P. Beyermann and Y. Yin, *Angew. Chem. Int. Edit.*, 2007, **119**, 4420-4423.
73 H. Q. Tao, K. Yang, Z. Ma, J. M. Wan, Y. J. Zhang, Z. H. Kang and Z. Liu, *small*, 2012, **8**, 281-290.